remote sensing

MDPI

Article

Dynamic Earthquake-Induced Landslide Susceptibility Assessment Model: Integrating Machine Learning and Remote Sensing

Youtian Yang [1,2,3], Jidong Wu [1,2,4,*], Lili Wang [1,2,3], Ru Ya [5] and Rumei Tang [5]

1 Joint International Research Laboratory of Catastrophe Simulation and Systemic Risk Governance, Beijing Normal University at Zhuhai, Zhuhai 519087, China; yangyoutian@mail.bnu.edu.cn (Y.Y.); wll1215@mail.bnu.edu.cn (L.W.)
2 School of National Safety and Emergency Management, Beijing Normal University, Beijing 100875, China
3 School of System Science, Beijing Normal University, Beijing 100875, China
4 Academy of Plateau Science and Sustainability, People's Government of Qinghai Province and Beijing Normal University, Xining 810008, China
5 Faculty of Geographical Science, Beijing Normal University, Beijing 100875, China; yaru@mail.bnu.edu.cn (R.Y.); tangrumei@mail.bnu.edu.cn (R.T.)
* Correspondence: wujidong@bnu.edu.cn

Abstract: Earthquake-induced landslides (EQILs) represent a serious secondary disaster of earthquakes, and conducting an effective assessment of earthquake-induced landslide susceptibility (ELSA) post-earthquake is helpful in reducing risk. In light of the diverse demands for ELSA across different time periods following an earthquake and the growing availability of data, this paper proposes using remote sensing data to dynamically update the ELSA model. By studying the Ms 6.2 earthquake in Jishishan County, Gansu Province, China, on 18 December 2023, rapid assessment results were derived from 12 pre-trained ELSA models combined with the spatial distribution of historical earthquake-related landslides immediately after the earthquake for early warning. Throughout the entire emergency response stage, the ELSA model was dynamically updated by integrating the EQILs points interpreted from remote sensing images as new training data to enhance assessment accuracy. After the emergency phase, the remote sensing interpretation results were compiled to create the new EQILs inventory. A high landslide potential area was identified using a re-trained model based on the updated inventory, offering a valuable reference for risk management during the recovery phase. The study highlights the importance of integrating remote sensing into ELSA model updates and recommends utilizing time-dependent remote sensing data for sampling to enhance the effectiveness of ELSA.

Keywords: earthquake-induced landslides; near-real-time optimization; spatial similarity; emergency management; integrated remote sensing

check for updates

Citation: Yang, Y.; Wu, J.; Wang, L.; Ya, R.; Tang, R. Dynamic Earthquake-Induced Landslide Susceptibility Assessment Model: Integrating Machine Learning and Remote Sensing. *Remote Sens.* **2024**, *16*, 4006. https://doi.org/10.3390/rs16214006

Academic Editors: Francesca Ardizzone and Michele Saroli

Received: 7 September 2024
Revised: 4 October 2024
Accepted: 24 October 2024
Published: 28 October 2024

Copyright: © 2024 by the authors. Licensee MDPI, Basel, Switzerland. This article is an open access article distributed under the terms and conditions of the Creative Commons Attribution (CC BY) license (https://creativecommons.org/licenses/by/4.0/).

1. Introduction

Earthquake-induced landslides (EQILs) are among the most prevalent and devastating secondary disasters associated with earthquakes [1]. The northeastern margin of the Qinghai-Tibet Plateau in China is particularly susceptible to these events, with over one-third of EQILs worldwide occurring in this region [2,3]. The Wenchuan earthquake, for instance, triggered over 60,000 EQILs, leading to a tragic loss of over 20,000 lives [4].

The threat of EQILs extends beyond the initial main shock of an earthquake. Aftershocks can also trigger EQILs, and the effects of seismic loosening and instability can persist for a significant duration [5]. Hence, the analysis of landslides following an earthquake is divided into two stages: the emergency response phase and the recovery stage. The first stage requires the earthquake-induced landslide susceptibility assessment (ELSA) immediately after the earthquake, within the hours and days, to offer crucial warnings

to rescue workers and affected residents [6]. For example, the United Nations response framework following a disaster mandates an initial assessment after 72 h and a second after 2 weeks [7,8]. The second phase, which may be delayed for weeks after the earthquake [9], aims to precisely pinpoint the locations of EQILs and provide valuable information for risk reduction strategies and environmental governance.

Broadly, there are three main types of ELSA approaches commonly used: physics-based models, statistical analysis models, and machine learning (ML) models [10]. Physics-based models thoroughly consider the earthquake-landslide mechanism and utilize the analysis results of slope instability mechanisms and sliding processes to quantitatively classify landslide susceptibility [11–13]. The application scale has been expanded from monolithic landslides to regional hazard assessments [14–17]. Both statistical analysis methods and machine learning models are empirical models, using EQIL inventories to establish the relationship between landslides and their influencing factors and extend the relationship to the entire research area [18]. The influencing factors generally fall into two categories. The first category is dynamic, encompassing ground motion factors such as Peak Ground Acceleration (PGA), Peak Ground Velocity (PGV), etc. The second category is static, reflecting the characteristics of the region itself, including geological, topographic, hydrological, and environmental attributes [5,10,19]. Formula reasoning is the main concern of statistical models [20]. With the advancement of GIS technology, statistical analysis models have rapidly evolved and been applied to numerous seismic events [21–23]. Machine learning models are increasingly being utilized, as they do not necessitate complex and rigorous physical processes found in mechanistic models [10] and can alleviate the dependency of statistical models on regular functions, enabling better resolution of nonlinear problems such as ELSA [20,24].

When employing a machine learning model to produce susceptibility maps for emergency response, the training dataset can consist of a compilation of landslide occurrences triggered by multiple earthquakes, such as on a global scale [23,25,26] or a smaller subset of earthquake-affected areas [8]. Here, we refer to these two training set types as "multiple" and "same-event" models, respectively. Logistic regression (LR) [23,26,27] and random forest (RF) algorithms [28–30] are the most commonly utilized methods in machine learning models for this purpose. For regional scales, certain machine learning algorithms, such as gradient boosting, have enhanced the accuracy of ML models [31]. Nevertheless, the results of these rapid assessments are highly uncertain due to the spatial heterogeneity and complexity of the affected areas [32]. In practical terms, the choice and combination of ML algorithms and training samples significantly influence the evaluation results [33,34]. The applicability of models in earthquake-affected areas will impact the reliability of the evaluation outcomes; thus, finding the most suitable model for any given case is a challenge [19]. Fortunately, regional ELSA is more focused on relative susceptibility and can judge the realism of the assessment based on past experience and regional conditions [35]. Even if the region lacks a complete EQIL inventory or has only a few records, which is the norm, the historical earthquake-related landslides record can be used as a reference for model selection [36].

In the short term (within 2 weeks) after the earthquake, the needs of disaster managers shift toward more detailed information. As Fan et al. [29] revealed in their study, the controls of post-seismic debris remobilizations are evolving rapidly, suggesting that susceptibility models based on a static time-related EQIL inventory may not accurately assess post-earthquake conditions. In other words, a model trained on data from a specific point in time may falter in the short term, necessitating dynamic updates according to new data. Remote sensing (RS) data comprises optical satellite images and synthetic aperture radar (SAR) data from satellites, which have proven to be valuable in identifying EQILs. Optical images can directly identify the locations of EQILs [37–39], although their spatial coverage may be limited by cloud cover and satellite revisit periods [40,41]. In commonly used optical imaging satellites, the Landsat-7 and Landsat-8 revisit cycles occur every 16 days, which is over two weeks, while Sentinel-2 and ZiYuan-3 (ZY-3) revisit every 5 days.

With networked constellations like GaoFen-1 (GF-1 B/C/D) capable of reducing revisit periods to one day [41]. SAR data can be acquired in any weather conditions, offering superior spatial coverage and suitability for terrain analysis [10,40,42]. When the optical image is significantly obscured by clouds, SAR data can offer additional information. The potential application of SAR in swiftly generating EQIL distribution maps for emergency response has been showcased in individual landslides or catchment areas, although with limited success [43,44]. In general, satellite images can be acquired within hours or days of an earthquake, and comparative analysis results based on images taken before and after a disaster can pinpoint actual EQIL locations, thereby establishing a data foundation for updating the susceptibility model.

Addressing the aforementioned challenges and the practical need for EQIL-related information post-earthquake, this paper proposes a dynamic detection model for EQILs that integrates machine learning and remote sensing images. Shortly after the earthquake, the most reliable ML model and its corresponding evaluation results are selected from a range of ELSA models trained on historical landslide inventories. This process aims to provide immediate predictive results regarding the spatial distribution of EQIL susceptibility shortly after the earthquake. Within two weeks of the earthquake, the identified EQILs are incorporated into the foundational training data through the interpretation of RS images, enabling near-real-time model updates to continually furnish more precise assessment outcomes to emergency response teams. After the emergency response phase, the comprehensive identification results of EQILs from RS images are compiled into the "single event" dataset for this earthquake. Building upon this dataset, the ELSA model is reconstructed, and the resulting evaluation outcomes for local EQILs are provided to inform subsequent risk management efforts.

2. Materials and Methods

2.1. Study Area

On 18 December 2023, a destructive earthquake (MS 6.2) struck Jishishan County, Gansu Province, at Beijing time of 23:59 (UTC 15:59, 18 December). The Jishishan earthquake is located at 102.79°N, 35.70°E, with a hypocentral depth of 10 km. The largest slip is located approximately 6.3 km NNW of the epicenter, the highest instrumental intensity is IX-X on the Mercalli scale, and the aftershocks are mostly distributed in the northwest direction within 20 km of the epicenter [45]. The Jishishan earthquake had a shallow focal point and occurred in the transition zone between the Qinghai-Tibet Plateau and the Loess Plateau (Figure 1). In this region, the soil layer was thick, and the altitude was high, leading to a noticeable amplification effect of seismic energy, resulting in significant surface damage [46,47]. The Jishishan earthquake impacted 772,000 individuals in Gansu and Qinghai provinces, resulting in the loss of 151 lives and injuries to 983 people. The disaster led to the collapse of 70,000 houses, severe damage to 99,000 houses, and general damage to 252,000 houses. The direct economic loss was estimated at CNY 14.612 billion (https://www.mem.gov.cn/xw/yjglbgzdt/202401/t20240120_475696.shtml, accessed on 20 January 2020).

The Jishishan seismogenic fault serves as the southern margin of LJSF, which has been active since the late Pleistocene to the Holocene [48]. Within 200 km of the epicenter of the Jishishan earthquake, there have been 2 earthquakes of magnitude 6.0 to 6.9 and 14 earthquakes of magnitude 5.0 to 5.9 since 1949 (Figure 1a). The maximum slip of the Jishishan earthquake occurred approximately 6.3 km northwest of the epicenter, reaching a peak value of 0.12 m. The distribution of PGA exhibited a similar pattern, with the high-value area situated to the northwest of the epicenter (Figure 1b). Historical landslides induced by earthquakes are primarily concentrated in loess hills with relatively low elevations and erosion-denudation hills in the region (Figure 1b). Loess covers a significant portion of the area, predominantly in the form of ridges and hilly terrain. Furthermore, human engineering activities in the area are substantial, and the practice of cutting slopes for

constructing houses and roads is prevalent, altering the natural slope morphology and contributing to landslide disasters in this area [49].

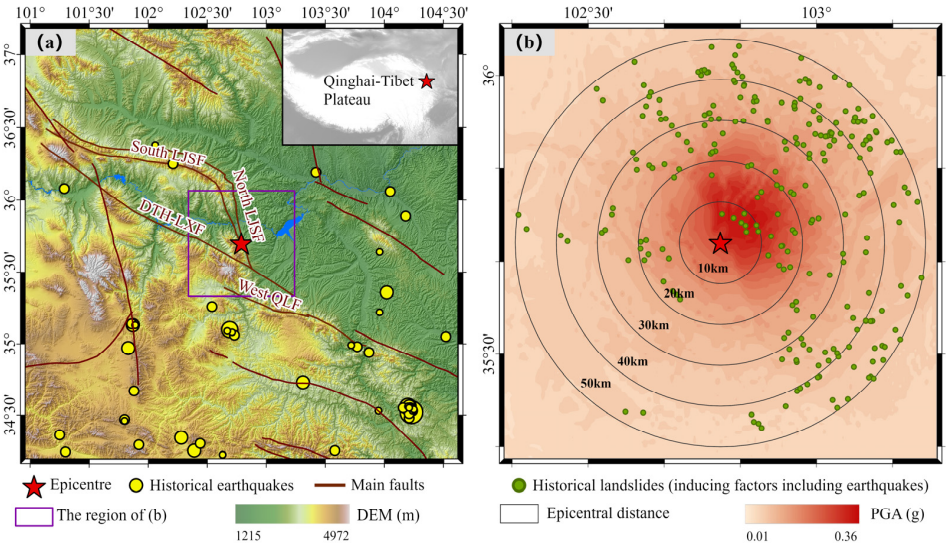


Figure 1. Tectonic, geomorphic setting, and historical disaster of the Jishishan Earthquake. (**a**) Tectonic background map of the Jishishan earthquake area. (**b**) Distribution of PGA and historical landslides (inducing factors, including earthquakes) within 50 km of the epicenter of the Jishishan earthquake. LJSF: Lajishan fault, RYSF: Riyueshan fault, QLF: Qinling fault, DTH-LXF: Daotanghe-Linxia fault.

2.2. Data Overview

2.2.1. EQIL Inventories

The initial training dataset for the rapid post-earthquake ELSA model includes 4 EQIL inventories from 4 historical seismic events that occurred on the eastern margin of the Qinghai-Tibet Plateau (TPE). These events include Dingxi (Ms 6.6, 22 July 2013), Wenchuan (Ms 8.0, 12 May 2008), Ya'an (Ms 7.0, 20 April 2013) and Luding (Ms 6.8, 5 September 2022) (Figure 2). The number of EQILs in the Dingxi inventory is 2330 [37], followed by 197,481 in Wenchuan [50], 15,546 in Ya'an [51], and 5007 in Luding [42]. These inventories originate from the Worldwide Database of Earthquake-Induced Landslide Inventories [52], which is widely used in various studies of EQILs [3,22,23,26,30].

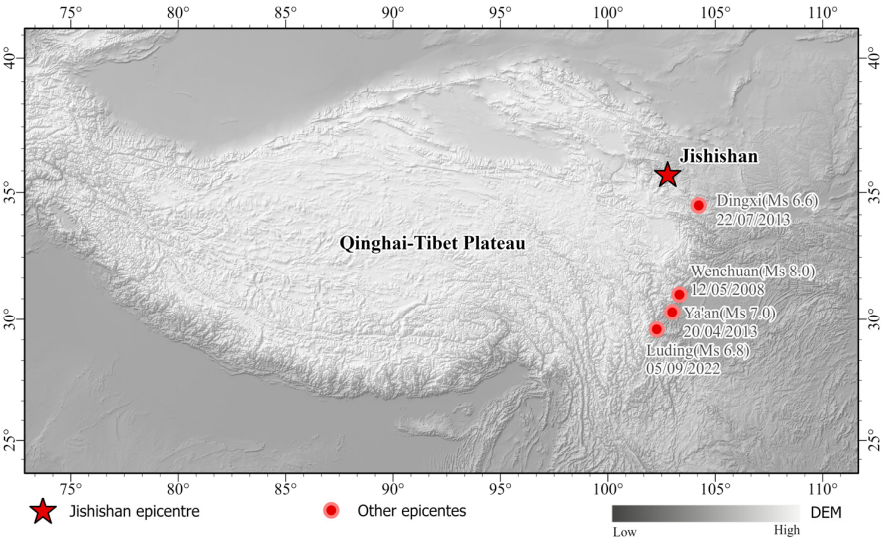


Figure 2. Location of the epicenter of the Dingxi, Wenchuan, Ya'an, and Luding earthquakes.

2.2.2. Influencing Factors

Based on previous research and an understanding of the mechanisms behind EQIL occurrences, this study selected 18 factors associated with the occurrence of EQILs [3,5,10]. These factors can be categorized into two groups. The first is triggering factors, which involve external driving forces exerted by ground motions, expressed in terms of Peak Ground Acceleration (PGA), Peak Ground Velocity (PGV), and Modified Mercalli Intensity (MMI); these data are available from the USGS ShakeMap shortly after the earthquake. The second perspective includes four types of static predisposing factors that are linked to local circumstances. These include the following: (1) Geology and soil: lithology, soil texture, and distance to fault; (2) Topography: elevation, slope, plane curvature, profile curvature, local relief, and Vegetation Removal Measure (VRM), calculated using Digital Elevation Models (DEMs); (3) Hydrology: distance to stream, Height Above the Nearest Drainage (HAND), and Topographic Wetness Index (TWI); and (4) Land use: Land Use and Land Cover (LULC), distance to road, and the Normalized Difference Vegetation Index (NDVI). Detailed data sources and descriptions of influencing factors are shown in Table 1. We resampled all data to 30 m to maintain consistent spatial resolution.

Table 1. Data sources and descriptions of factors.

Groups	Factors	Source	Spatial Resolution
Seismic	PGA	USGS ShakeMap (https:/earthquake.usgs.gov/data/shakemap, accessed on 19 December 2023)	Vector Data
	PGV		Vector Data
	MMI		Vector Data
Geology and soil	Distance to fault	Calculated based on active structure map of China [53]	Vector Data
	Soil texture	ISRIC-Soil and landform properties for LADA partner countries [54]	Vector Data
	Lithology		Vector Data
Topography	Elevation (DEM)	STRM (http://srtm.csi.cgiar.org, accessed on 23 February 2023)	30 m
	Slope	Calculated based on DEM	30 m
	Plan curvature		
	Profile curvature		
	Local relief		
	VRM		
Hydrology	HAND	MERIT Hydro: global hydrography datasets [55,56]	90 m
	Distance to stream	Calculated based on MERIT Hydro	Vector Data
	TWI	Calculated based on DEM	90 m
Environmental	Distance to road	Calculated based on roads data from OSM (http://www.openstreetmap.org, accessed on 3 August 2023)	Vector Data
	NDVI	MOD13A3 (http://doi.org/10.5067/MODIS/MOD13A3.006, accessed on 19 December 2023)	1 km
	LULC	GLC_FCS30 [57]	30 m

2.2.3. Remote Sensing Images and Other Data

The optical satellite images used to interpret EQILs are sourced from the Gaofen-1 (GF-1) satellite, utilizing pre-earthquake images captured on 18 December and post-earthquake images taken on 19 December. The GF-1 satellite is equipped with two 2 m

resolution panchromatic and 8 m resolution multispectral cameras, offering a single-star revisit period of 4 days; the revisit period was shortened by 1 day after networking in 2018 (https://www.cresda.com/zgzywxyyzx/index.html, accessed on 24 February 2022). Historical landslide data are sourced from the Atlas of Natural Resources in the Middle and Upper Reaches of the Yellow River [58]. It is worth noting that the historical landslide disaster records encompass various inducing factors, such as rainfall, excavation, earthquake, weathering, etc. The inducing factors of some historical landslide records are not singular, so the relevant records including the inducing factor "earthquake" are selected as historical earthquake-related landslides, which regarded as historical EQILs. Points of potential landslides, whose deformation is intensified by the Jishishan earthquake, come from the results of a post-earthquake geological disaster field investigation [49].

2.3. Overview of the Approach

This paper focuses on ELSA at various stages following an earthquake. These stages can be categorized into the emergency response phase, including two assessment periods: immediately to 72 h after the earthquake and two weeks after the earthquake. Additionally, it covers the recovery phase, spanning from two weeks to several months after the earthquake.

As shown in Figure 3, within 72 h of the earthquake, 12 models pre-trained using 4 machine learning methods—random forest, deep forest, GBDT, and XGBoost—along with 3 types of sample sets, "all samples", "equal samples", and "nearest neighbor samples" (samples of adjacent seismic events), were employed to conduct a preliminary ELSA in the disaster area. Leveraging historical landslide data, a similarity perception algorithm was utilized to identify the best outcome from the 12 preliminary results, serving as the initial rapid result, and the corresponding ML model was selected as the model with the best regional applicability. During the period of 2 weeks after the earthquake, as the interpretation of remote sensing images may not be finalized or the results have not been verified, this paper utilizes real EQILs extracted from certain remote sensing images as new samples to optimize the model in order to approximate the actual situation. Throughout this process, the model evaluation results are updated in near real time alongside the interpretation results of remote sensing images. In the recovery stage (two weeks later), upon completion of remote sensing image interpretation, the EQIL extraction results from this earthquake were utilized to construct an EQIL inventory, which served as a training set ("same-event" training set) to retrain the ML model. The ML model with the most favorable performance, as determined by the AUC value and ROC curve, was selected to conduct more precise ELSA.

In this process, we employ visual interpretation to identify earthquake-induced landslides, as we prioritize reliability as the primary factor for technical support during actual disaster response. Following radiometric calibration, atmospheric correction, and orthorectification of the GF-1 image using ENVI remote sensing software (v5.6), band fusion is performed using the GS panchromatic sharpening image fusion algorithm [57] to finally obtain an image with a spatial resolution of 2 m. We identify EQILs through human visual contrast interpretation in ArcGIS Pro (v3.0.2) by comparing preprocessed optical satellite images before and after earthquakes. As a result of variations in the timing of acquiring and processing remote sensing data, ongoing model updates during interpretation assist in mitigating delays in evaluation results caused by processing extensive remote sensing data.

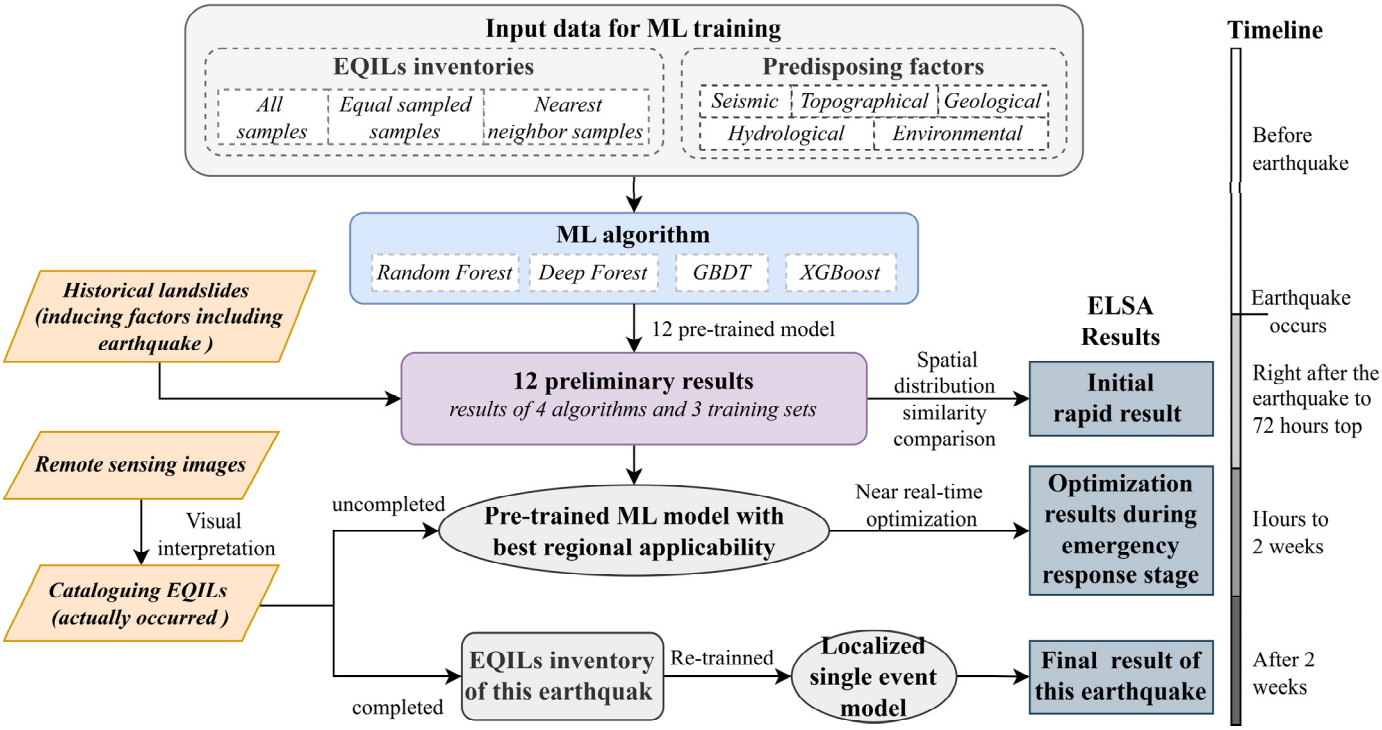


Figure 3. Schematic overview of the methods and data utilized in this study.

2.4. Pre-Trained Model for Preliminary Results

Tree-based models are popular in various domains because of their efficiency and cost-effectiveness [20,32]. These models have several advantages, such as requiring minimal data preprocessing, not needing standardization or normalization, and being able to handle both continuous and categorical variables. Several integrated and optimized models have been developed for tree-based models. In this paper, the focus is on selecting four widely used and effective algorithms for model construction [20,30,34,59].

(1) Random Forest (RF): The random forest is a typical Bagging-based ensemble model that consists of several decision trees as basic units and synthesizes these homogeneous weak classifiers with certain rules to form a strong classifier [36].
(2) Deep Forest (DF): Deep forest is also known as gcForest (Multi-Grained Cascade Forest); it is similar to the idea of neural networks but has lower requirements for hyperparameters, and the complexity of the model can be adaptive and extensible [60].
(3) Gradient Boosting Decision Tree (GBDT): It takes a decision tree as its basic unit; the core idea is to use the value of the negative gradient of the loss function in the current model as the approximate value of the residual, so that the loss function can be rapidly reduced.
(4) eXtreme Gradient Boosting (XGBoost): XGBoost is further modified based on the GBDT model. These optimizations help prevent overfitting and improve generalization ability [61].

In the selection of pre-training samples, three sets of samples were used for model training. The first set, "All samples", consists of all samples from the EQIL inventories near the eastern margin of the Qinghai-Tibet Plateau. The second set is "equal samples", where an equal number of samples from each EQIL inventory were combined to eliminate the impact of sample amount differences on the model. The third set is the "nearest neighbor samples", where samples from nearby regions were considered. This is because regions with close spatial distance often have similar environmental conditions, and the EQIL characteristics of nearby neighbors may provide valuable references. In this paper, the nearest inventory is the Dingxi inventory (we shall hereafter refer to it as Dingxi samples),

where the affected area is also in the transition zone from the Qinghai-Tibet Plateau to the Loess Plateau.

To ensure that each sampling point of the landslides is located within the boundary of the landslide, we converted the polygons into points and assigned a label value of "1" to points located within the landslide area, and "0" to points outside the landslide area [30]. We constructed a balanced training set (80%) and test set (20%), meaning the dataset contained an equal number of landslide and non-landslide points to ensure geographic representation [36,62,63]. During the training process, 10-fold cross-validation was employed to optimize the model parameters, resulting in Area Under Curve (AUC) values exceeding 0.95 for all 12 models on their respective test sets.

2.5. Spatial Distribution Similarity Comparison

Due to the historical EQILs consisting of spatially discrete points, direct comparison with the ML model outputs (raster) is not feasible. Meanwhile, different ML algorithms use distinct methods to estimate the probability, making the output results indirectly comparable across various ML algorithms [32,64]. Therefore, we compared the spatial distribution patterns of historical EQILs and ML preliminary outputs for similarity and then selected the optimal result as the initial rapid result.

In the field of computer vision, there are many techniques used to evaluate image similarity, such as the histogram method [65], cosine similarity method [66], and hash method [67], which have been applied in map similarity matching [68]. To enable comparison of regions as a whole rather than individual points or pixels, we opted for the global hashing algorithm and histogram method for similarity comparison. The Hash algorithm is commonly used in computer vision to measure the similarity between images. It involves generating a feature string for each image by analyzing its pixels and then comparing these feature strings to determine the degree of similarity between images. There are different variations of the Hash algorithm based on how the feature string is generated: (1) Average Hash Algorithm (aHash): This algorithm compares each pixel of an image with the average value of all pixels in the image. (2) Difference Hash Algorithm (dHash): In this algorithm, each pixel is compared with the previous pixel in the same row of the image. (3) Perceptual Hash Algorithm (pHash): This algorithm compares each pixel of an image with the mean value of pixels in a window after applying cosine transformation [69]. Histogram statistics involve comparing the distribution of pixel values in either the RGB three-channel or gray single-channel histograms; unlike Hash algorithms, this approach focuses more on the overall distribution of pixel values [69].

We partitioned the disaster area, using the epicenter of the Jishishan earthquake as the center and a 50-km radius, into 80 sub-areas, each with a 22.5-degree angle and a radial distance of 10 km. For each subregion, compute the point density of historical EQILs and the percentage of grids where EQILs (labeled as "1" in the ML model output) are probable. Then, the quantile method (10th percentile) was employed to create spatial distribution maps of EQIL susceptibility on a subregional basis. By employing 3 Hash algorithms (aHash, dHash, and pHash) and 2 histogram statistical methods (single channel and three channel), the study compared the spatial distribution similarity between historical EQILs and each output. As there can be significant differences between these two types of methods, we calculate the average of the 3 Hash algorithms and the average of all 5 algorithms as the criteria for similarity evaluation. In this context, a smaller value indicates a higher degree of similarity.

3. Results

3.1. Immediate EQIL Susceptibility Assessment and Model Selection

The preliminary results of the EQILs' spatial distribution of the Jishishan earthquake using 12 pre-training models are shown in Figure 4. These results are in the form of raster images with a spatial resolution of 30 m. Through a comparison of these 12 prediction results, it becomes evident that both the training samples and the algorithms significantly

influence the prediction outcomes. However, the spatial distribution pattern is primarily determined by the training samples (each row in Figure 4), while the specific value of the susceptibility probability produced by the model varies according to the algorithm utilized (each column in Figure 4).

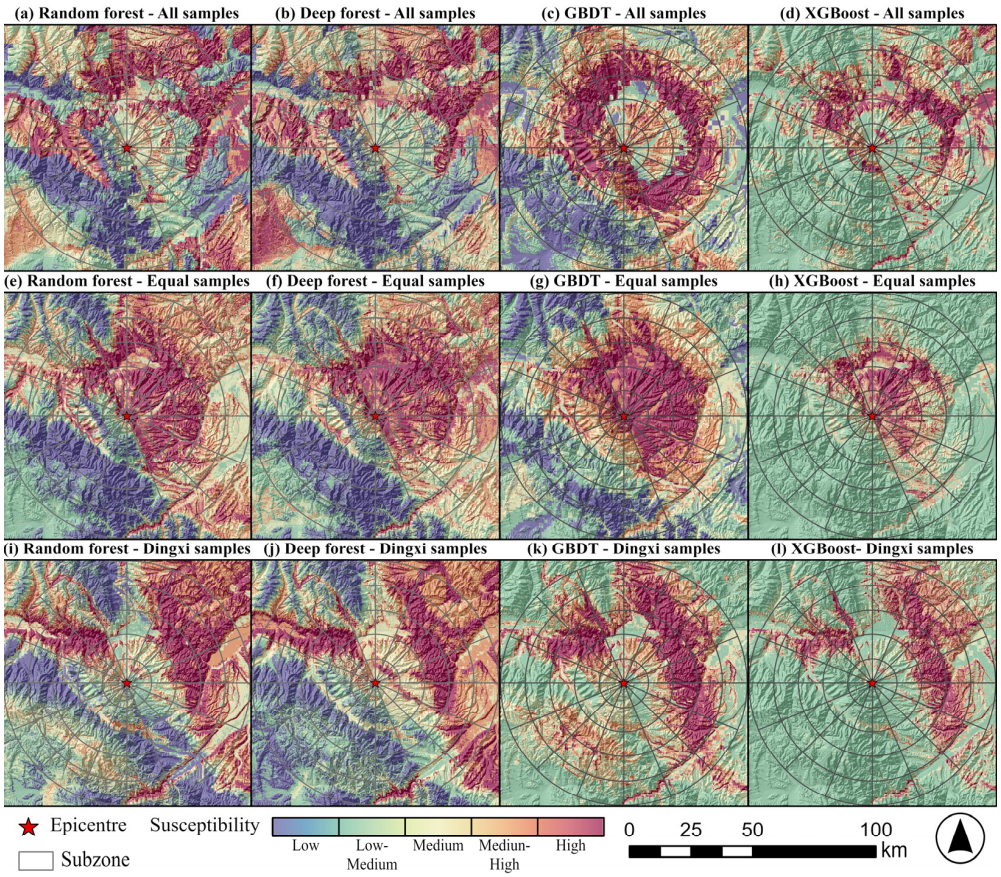


Figure 4. Preliminary results of EQIL susceptibility of the Jishishan earthquake using 12 pre-training models. Relative susceptibility in each subgraph was determined by the quantile method (20% quantile). Subgraphs with identical columns utilize the same machine learning outputs, while subgraphs with matching rows utilize the same training data.

The comparison of four ML algorithms reveals that RF and DF exhibit a higher tolerance for EQIL determination, with broader coverage of high susceptibility. On the other hand, GBDT and XGBoost have stricter determination conditions and a more concentrated range of assessed high susceptibility. While the spatial pattern distribution of various training samples generally exhibits a higher concentration in the northeast direction, there are notable differences in the detailed distribution. The high-susceptibility areas associated with "All samples" are primarily clustered in the north and northeast directions, extending over distances exceeding 20 km. In contrast, the outcomes based on "Equal samples" are focused in the northeast direction but within a narrower range of less than 30 km. The findings from the "Dingxi samples" display a scattered distribution with a southwest direction being more susceptible compared to the other datasets.

To identify the 12 preliminary results that are most likely to align with the local situation and are most beneficial for earthquake relief efforts, we conducted a comparison of the similarity between the preliminary results and the spatial distribution pattern of historical EQILs (Figure 5).

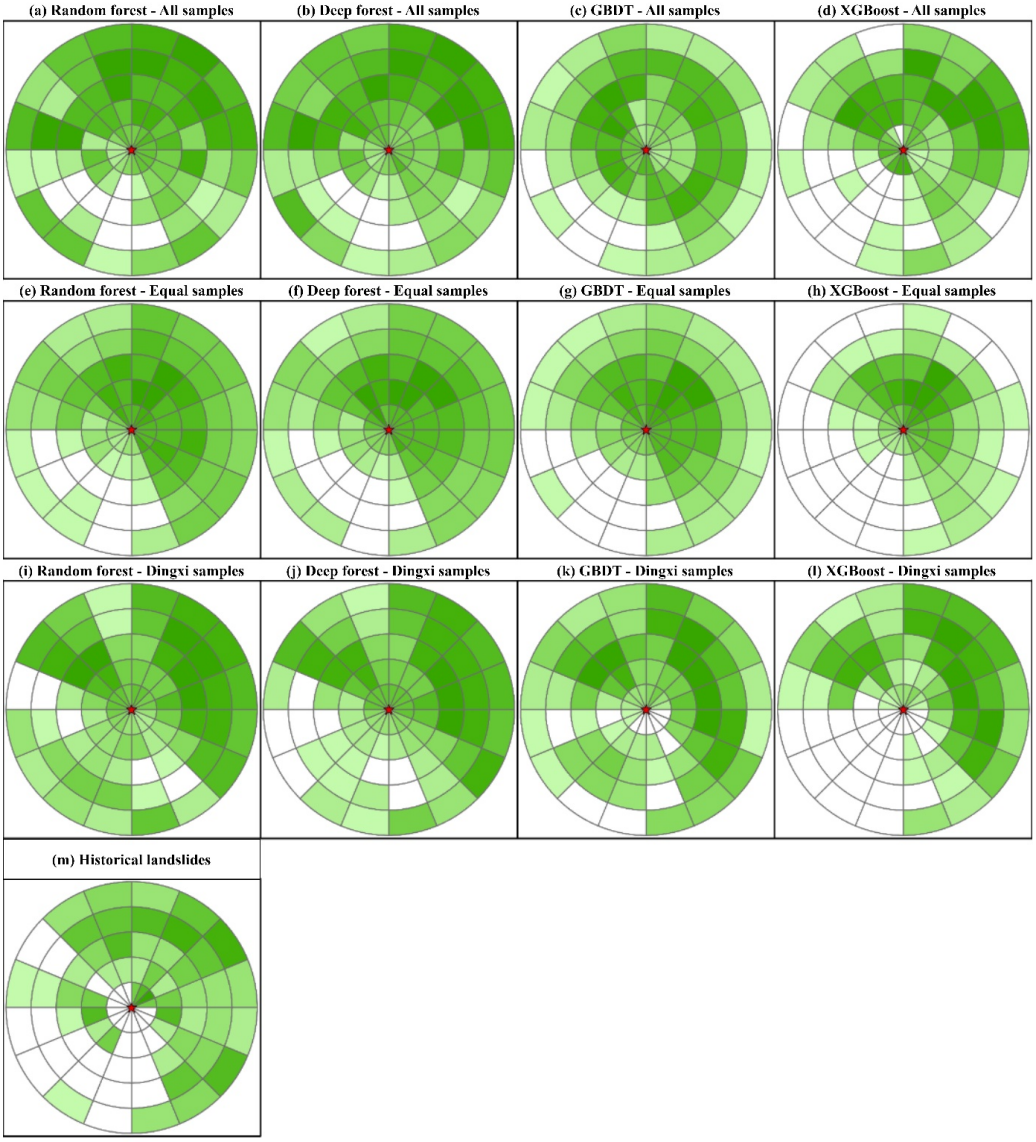


Figure 5. Spatial distribution pattern of historical EQILs and 12 preliminary results. The red star is the location of the epicenter of the Jishishan earthquake. Green color from light to deep indicate low to high landslide susceptibility (12 results) and EQILs density (historical).

Due to the distinct principles underlying the histogram statistical algorithm and the Hash algorithm, neither holds a definitive advantage over the other. As a result, this study utilizes both histogram statistics and the Hash algorithm to calculate similarity (Table 2), as well as solely the Hash algorithm (Table 3). The findings from both algorithms indicate that assessments based on "Equal samples" demonstrate the highest similarity with the spatial distribution of historical landslide disasters. The discrepancy arises in the former identifying the "Random forest—Equal samples" combination as displaying the highest similarity, while the latter favors the "XGBoost—Equal samples" combination. Ultimately, a combined average of the two initial evaluation outcomes is chosen as the primary rapid assessment result for post-earthquake rescue operations.

Table 2. Comparison of similarities: Histogram statistics and Hash algorithm.

	Random Forest	Deep Forest	GBDT	XGBoost	Mean
Total samples	0.677	0.681	0.696	0.698	0.688
Equal samples	0.670	0.680	0.692	0.698	0.685
Dingxi samples	0.687	0.683	0.713	0.724	0.702
Mean	0.678	0.681	0.700	0.707	

Table 3. Comparison of similarities: Hash algorithm.

	Random Forest	Deep Forest	GBDT	XGBoost	Mean
Total samples	0.875	0.885	0.871	0.864	0.874
Equal samples	0.877	0.882	0.862	0.842	0.866
Dingxi samples	0.867	0.872	0.865	0.874	0.870
Mean	0.873	0.880	0.866	0.860	

3.2. Near-Real-Time Model Optimization Integrating Remote Sensing Interpretation

The initial rapid results may differ from the actual locations of EQIL occurrences. Therefore, it is crucial to update ELSA assessments during the emergency response phase to ensure they provide more valuable information for rescue operations. The variation among the 12 preliminary outputs underscores the substantial impact of the training set on the evaluation results. Thus, the study incorporates remote sensing image interpretations to supplement the training set. The visual interpretation of EQIL remote sensing images for the Jishishan earthquake is depicted in Figure 6 (green). A total of 1427 landslides were identified, primarily distributed in the northeast direction of the epicenter. Most of these were small to medium-sized loess landslides, with some being shallow surface rock collapses. The Equal—Random Forest and Equal—XGBoost models, which initially showed promising results, were subsequently retrained using this additional data. In the week following the earthquake, we continuously updated the model as the actual landslide locations were identified. Figure 6 presents a comparison of the final updated results (Figure 6b) with the initial evaluation results of the "Random Forest—Equal" and "XGBoost—Equal" fusion results (Figure 6a), along with the occurrence locations of EQILs obtained from remote sensing within 2 weeks after the earthquake.

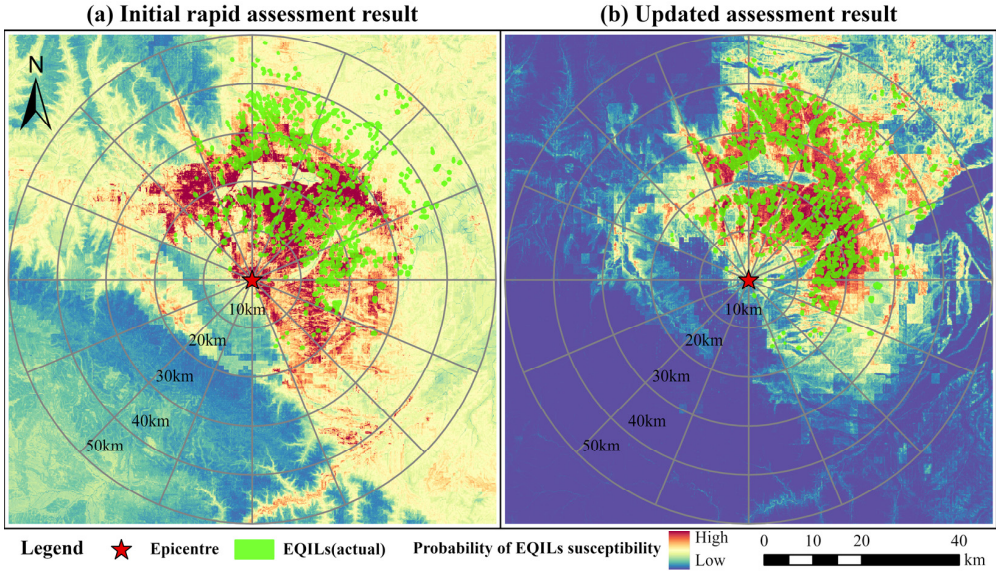


Figure 6. Comparison of initial rapid assessment results and final update results with actual EQIL locations interpreted through remote sensing images.

While the initial rapid assessment results exhibit a similar spatial distribution trend to the actual occurrence locations of EQILs, there are some deviations in the detailed estimations. The most notable discrepancy is the overestimation of EQIL occurrence by 10–20 km to the northwest and southeast of the epicenter, and the underestimation by more than 30 km to the northeast. The updated model shows significant improvements in correcting these three deviations. In particular, it accurately identifies a majority of EQILs in areas located over 30 km northeast of the epicenter. Furthermore, the landslide susceptibility in the vicinity of the epicenter (within a 5-km radius) has been greatly diminished, aligning with the actual conditions of the Jishishan earthquake.

In addition to the visual representation of spatial distribution, which effectively demonstrates the enhancement of the model's performance, the Receiver Operating Characteristic (ROC) curve and Area Under Curve (AUC) values depicted in Figure 7 provide a quantitative measure of this improvement. Both algorithms witnessed a notable increase of 0.1 in their respective AUC values. What is even more remarkable is the significant improvement in the Accuracy (ACC) value, with the random forest model experiencing an increase of 0.4, while the XGBoost model saw a commendable improvement of 0.37.

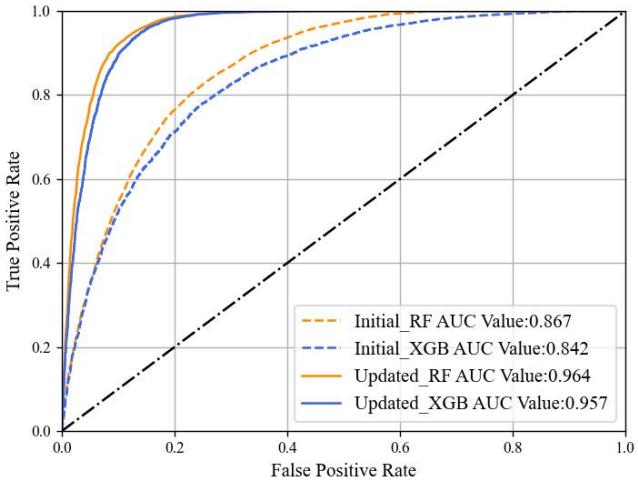


Figure 7. ROC curve of the initial model and the updated model.

3.3. Localization Model Reconstruction Based on New EQIL Inventory

As the relief efforts for earthquake disasters and relocation draw to a close, the attention surrounding EQILs will shift toward identifying areas with an increased possibility of slope instability. This transition necessitates a higher level of precision in regional ELSA models. With the allocation of human resources and the availability of high-resolution remote sensing images, numerous real EQILs were identified and recorded. At this stage, a sufficient amount of data has been gathered to construct ELSA models that are more finely tailored to the characteristics of the earthquake event. We integrated all identified actual EQILs based on remote sensing images (referred to as the local data) into an inventory of EQILs for the Jishishan earthquake and used it as a new training dataset.

Table 4 presents the AUC values and ACC values on the test set using four machine learning algorithms, the local dataset from Jishishan for model training, and two optimization models. Among all the models, the Deep Forest-Jishishan model stands out as the most effective (Figure 8a), with an AUC value of 0.991. Notably, the AUC value of the Random Forest—Equal Samples model, generated through continuous updating, has surpassed that of the GBDT model utilizing local data. This finding further validates the reliability of the near-real-time updating model. However, the average accuracy of the model employing local data still exceeds that of the optimized model. This suggests, on one hand, that EQIL evaluation is significantly influenced by the spatial heterogeneity of geographical environmental conditions. On the other hand, it highlights the need to establish a comprehensive

database for each disaster event to adequately prepare for potential disasters that may occur in neighboring regions in the future.

Table 4. Precision comparison between the localized model and the updated model.

Model—Training Samples	Model Type	AUC	ACC
Random Forest—Jishishan	Localization model	0.989	0.959
Deep Forest—Jishishan	Localization model	0.991	0.967
GBDT—Jishishan	Localization model	0.962	0.918
XGBoost—Jishishan	Localization model	0.985	0.957
Random Forest—Equal samples	Updated model	0.964	0.911
XGBoost—Equal samples	Updated model	0.957	0.904

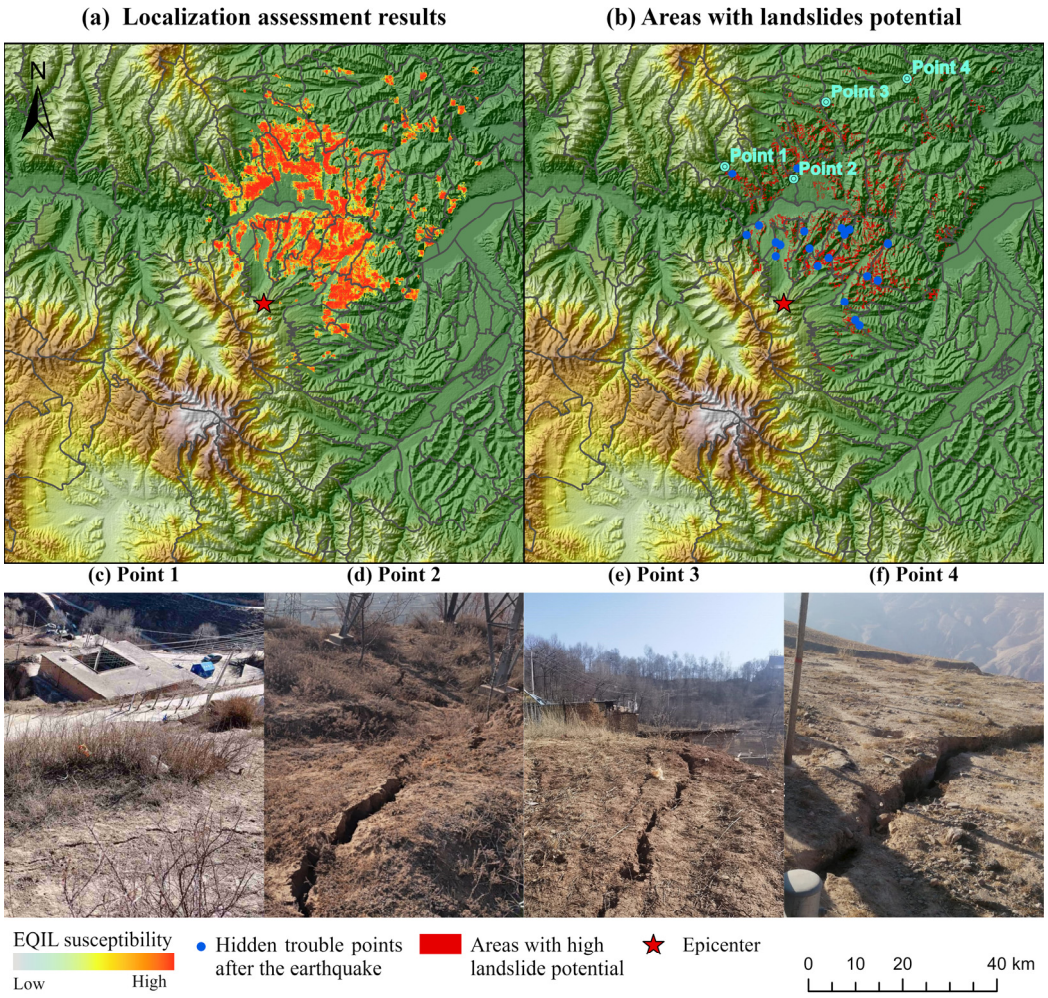


Figure 8. Localized model ELSA results (**a**) and areas with high landslide potential (**b**). (**c**–**f**) are field investigation photos of points 1–4.

The stabilization of the affected areas can be a time-consuming process, making it a long-term effort to reduce the likelihood of landslides occurring after an earthquake. Building upon this, for future disaster management and risk reduction efforts, we identified areas labeled by the model as high EQIL susceptibility that are currently not experiencing EQILs (Figure 8b).

Apart from the areas already affected by landslide disasters, there is an additional area of high landslide susceptibility of approximately 152 square kilometers where EQILs may occur. Furthermore, there are hidden trouble points located more than 50 km northeast of the epicenter, close to the local reservoir area, that require attention. The areas of high

landslide susceptibility identified by the ELSA model cover most of the new hidden trouble points identified through field surveys. This information is crucial for targeted mitigation and resource allocation, reducing the impact of EQILs by focusing on certain areas without scanning the entire affected region.

4. Discussion

4.1. The Jishishan Earthquake May Raise the Possibility of Landslides

In addition to the EQILs that have already occurred, the heightened potential for landslides following the Jishishan earthquake demands continuous attention, especially in areas with instability or cracks in the ground, primarily caused by two reasons:

Firstly, the location of the Jishishan earthquake itself and the timing characteristics of the disaster's occurrence. The affected area of the Jishishan earthquake is at a high altitude, and the seismic event occurred during winter. Frozen soil or ground was observed in certain areas, which somewhat reduced the likelihood of earthquake-induced landslides. However, fluctuations in slope stability are synchronized with variations in soil volumetric water content and reach their maximum precisely at the peak of snowmelt [70]. As time progresses, the increasing temperatures are likely to serve as significant factors that incentivize the transformation of earthquake-induced unstable slopes into landslide disasters.

On the flip side, as a result of climate change, the 400 mm isohyet in China is shifting northwestward, leading to increased warmth and precipitation on the Loess Plateau and the northeastern edge of the Qinghai-Tibet Plateau [71]. This results in more frequent intense short-term and prolonged precipitation, exacerbating the risk of precipitation-triggered loess landslides. For instance, in Haidong City, Huzhu County, north of the Jishishan earthquake zone, a 577,000 square meter landslide occurred in September 2022 due to persistent rainfall, claiming seven lives. The Menyuan earthquake in May 2022 may have impacted the occurrence of that landslide [72]. As depicted in Figure 8c–f, the Jishishan earthquake has induced partial slope instability. With the potential for heavy rainfall in the future, residential structures, roads, and power infrastructure could all be at risk.

4.2. Deficiencies and Prospects

For the method proposed in this paper, we comprehensively selected 18 factors in the ML model. However, factors commonly used in physical models at the unit scale, such as sub-soil resistance and water table elevation, were excluded from the model due to data availability constraints. Undeniably, physical models often exhibit strong reliability in assessing the likelihood of slope-unit landslides [73]. At the regional scale, models based on the Newmark slider model are required to estimate the safety factor, FS, for each grid or slope unit [15,16]. The calculation of FS typically entails the strength parameters of soil and rock (the internal angle of friction and cohesion), which are largely unknown at the spatial scales associated with landslides [74]. While these parameters can be assumed (e.g., using a uniform internal friction angle) or estimated from other EQIL inventories using inversion methods, uncertainty still persists [35]. In other words, to some extent, both the physical analysis-based model and the ML model need to be updated for the region to reduce uncertainty. Due to insufficient geotechnical data, we were unable to compare the evaluation results of the machine learning model with those of the physical model.

When considering the regional scale and emergency response, the integration of machine learning and remote sensing images offers advantages. The ML method can ensure timeliness, while remote sensing can enhance the accuracy of the assessment work. As demonstrated in this paper, the results of remote sensing image interpretation can continuously optimize the applicability of ML models for specific seismic events in a convenient manner. In particular, the ability of remote sensing images to capture actual conditions after earthquakes has increased the relevance of models to reality, and this enhancement undoubtedly contributes to more effective disaster management practices. Additionally, this capability to adapt to real-time situations is especially valuable for disasters like

EQILs, where substantial changes can occur within a brief timeframe, rendering previous experiences partially inapplicable [29].

Furthermore, regarding model evaluation, this study assesses the performance of the initial models generated by four machine learning algorithms and three types of training samples. Theoretically, regions with similar geographical proximity exhibit higher resemblance, potentially leading to better model generalization for areas with akin feature characteristics. Regrettably, the Dingxi dataset chosen as the nearest neighbor sample in this study is approximately 200 km away from the Jishishan earthquake epicenter. Despite both locations lying in the transition zone between the Qinghai-Tibet Plateau and the Loess Plateau, they differ significantly in induced factors, particularly in hydrological and geological conditions. Consequently, the impact of spatial heterogeneity and factor selection on the ELSA model has not been extensively deliberated in this paper, warranting further exploration in future research.

5. Conclusions

To address the challenge of model selection for EQILs assessment in rapid post-earthquake emergency response and model optimization in subsequent risk mitigation, this study initially developed twelve assessment models using various combinations of machine learning algorithms and samples. The initial optimal model was determined by comparing the spatial similarity with historical disaster distribution. Subsequently, the model was optimized by reconstructing training samples using near real time remote sensing data. Finally, after obtaining a sufficient number of actual EQIL points, the localization model with the highest accuracy was determined. The main conclusions and findings of this paper are as follows:

(1) The impact of training samples on the results is more significant than the choice of machine learning algorithms. Given the distinctive characteristics of each disaster event, incorporating a wide range of samples during training may not always yield optimal results.

(2) The similarity perception obtained from historical earthquake-related landslides is beneficial for model selection, while the selected rapid assessments offer vital information for immediate post-earthquake emergency responses. The spatial distribution of historical landslides proves to be an effective method for quickly selecting prediction results.

(3) Updating the ELSA model through remote sensing during the emergency phase allows for the provision of near-real-time guidance to relevant stakeholders. Following the latest optimization, the model's accuracy has improved by 0.1 in AUC value and by 0.4 in ACC value compared to that of the initial model. It has been demonstrated that integrating remote sensing information is essential for emergency rescue operations following an earthquake.

(4) Establishing an EQIL inventory through remote sensing interpretation is advantageous for enhancing the accuracy of ELSA. Spatially, addressing the challenges presented by geospatial heterogeneity is difficult, and localized databases can serve as foundational data sources for improved local accuracy. Temporally, creating a new EQILs Inventory with remote sensing interpretation following an earthquake represents an effective update in the time dimension.

(5) The ELSA model which integrating machine learning and remote sensing and machine learning can reduce the cost of expensive field surveys in earthquake-affected areas. In future regional risk management processes, we can prioritize these areas and consider the impact of additional triggering factors, such as precipitation and human activities.

Author Contributions: Conceptualization, Y.Y. and J.W.; Data curation, L.W.; Investigation, J.W.; Methodology, Y.Y. and J.W.; Resources, R.Y. and R.T.; Validation, Y.Y.; Visualization, Y.Y.; Writing—original draft, Y.Y.; Writing—review and editing, J.W., L.W., R.Y. and R.T. All authors have read and agreed to the published version of the manuscript.

Funding: This research was funded by the National Key R&D Program of China (Grant No. 2022YFC3004404).

Data Availability Statement: No new data are generated in this study. The data used in this study are public-use data files prepared and disseminated to provide access to the full scope of the data. Data will be made available on request.

Conflicts of Interest: The authors declare no conflicts of interest. The funders had no role in the design of the study; in the collection, analyses, or interpretation of data; in the writing of the manuscript; or in the decision to publish the results.

References

1. Fan, X.; Juang, C.H.; Wasowski, J.; Huang, R.; Xu, Q.; Scaringi, G.; van Westen, C.J.; Havenith, H.-B. What We Have Learned from the 2008 Wenchuan Earthquake and Its Aftermath: A Decade of Research and Challenges. *Eng. Geol.* **2018**, *241*, 25–32. [CrossRef]
2. Deng, Q.D.; Cheng, S.-P.; Ma, J.; Du, P. Seismic Activities and Earthquake Potential in the Tibetan Plateau. *Chin. J. Geophys.* **2014**, *57*, 2025–2042. [CrossRef]
3. Zhao, B.; Su, L.; Xu, Q.; Li, W.; Xu, C.; Wang, Y. A Review of Recent Earthquake-Induced Landslides on the Tibetan Plateau. *Earth-Sci. Rev.* **2023**, *244*, 104534. [CrossRef]
4. Yin, Y.; Wang, F.; Sun, P. Landslide Hazards Triggered by the 2008 Wenchuan Earthquake, Sichuan, China. *Landslides* **2009**, *6*, 139–152. [CrossRef]
5. Fan, X.; Scaringi, G.; Korup, O.; West, A.J.; van Westen, C.J.; Tanyas, H.; Hovius, N.; Hales, T.C.; Jibson, R.W.; Allstadt, K.E.; et al. Earthquake-Induced Chains of Geologic Hazards: Patterns, Mechanisms, and Impacts. *Rev. Geophys.* **2019**, *57*, 421–503. [CrossRef]
6. Robinson, T.R.; Rosser, N.J.; Densmore, A.L.; Williams, J.G.; Kincey, M.E.; Benjamin, J.; Bell, H.J.A. Rapid Post-Earthquake Modelling of Coseismic Landslide Intensity and Distribution for Emergency Response Decision Support. *Nat. Hazards Earth Syst. Sci.* **2017**, *17*, 1521–1540. [CrossRef]
7. Humanitarian Programme Cycle. Available online: https://kmp.hpc.tools/ (accessed on 2 August 2024).
8. Heleno, S.; Matias, M.; Pina, P.; Sousa, A.J. Semiautomated Object-Based Classification of Rain-Induced Landslides with VHR Multispectral Images on Madeira Island. *Nat. Hazards Earth Syst. Sci.* **2016**, *16*, 1035–1048. [CrossRef]
9. Burrows, K.; Milledge, D.; Walters, R.J.; Bellugi, D. Integrating Empirical Models and Satellite Radar Can Improve Landslide Detection for Emergency Response. *Nat. Hazards Earth Syst. Sci.* **2021**, *21*, 2993–3014. [CrossRef]
10. Shao, X.; Xu, C. Earthquake-Induced Landslides Susceptibility Assessment: A Review of the State-of-the-Art. *Nat. Hazards Res.* **2022**, *2*, 172–182. [CrossRef]
11. Newmark, N.M. Effects of Earthquakes on Dams and Embankments. *Géotechnique* **1965**, *15*, 139–160. [CrossRef]
12. Bray Jonathan, D.; Travasarou, T. Simplified Procedure for Estimating Earthquake-Induced Deviatoric Slope Displacements. *J. Geotech. Geoenviron. Eng.* **2007**, *133*, 381–392. [CrossRef]
13. Huang, M.; Fan, X.; Wang, H. Three-Dimensional Upper Bound Stability Analysis of Slopes with Weak Interlayer Based on Rotational-Translational Mechanisms. *Eng. Geol.* **2017**, *223*, 82–91. [CrossRef]
14. Dreyfus, D.; Rathje, E.M.; Jibson, R.W. The Influence of Different Simplified Sliding-Block Models and Input Parameters on Regional Predictions of Seismic Landslides Triggered by the Northridge Earthquake. *Eng. Geol.* **2013**, *163*, 41–54. [CrossRef]
15. Gallen, S.F.; Clark, M.K.; Godt, J.W.; Roback, K.; Niemi, N.A. Application and Evaluation of a Rapid Response Earthquake-Triggered Landslide Model to the 25 April 2015 Mw 7.8 Gorkha Earthquake, Nepal. *Tectonophysics* **2017**, *714–715*, 173–187. [CrossRef]
16. Jibson, R.W.; Harp, E.L.; Michael, J.A. A Method for Producing Digital Probabilistic Seismic Landslide Hazard Maps. *Eng. Geol.* **2000**, *58*, 271–289. [CrossRef]
17. Wang, T.; Wu, S.; Shi, J.; Xin, P. Case Study On Rapid Assessment of Regional Seismic Landslide Hazard Based On Simplified Newmark Displacement Model: Wenchuan Ms 8.0 Earthquake. *J. Eng. Geol.* **2013**, *21*, 16–24. [CrossRef]
18. Guzzetti, F.; Carrara, A.; Cardinali, M.; Reichenbach, P. Landslide Hazard Evaluation: A Review of Current Techniques and Their Application in a Multi-Scale Study, Central Italy. *Geomorphology* **1999**, *31*, 181–216. [CrossRef]
19. Reichenbach, P.; Rossi, M.; Malamud, B.D.; Mihir, M.; Guzzetti, F. A Review of Statistically-Based Landslide Susceptibility Models. *Earth-Sci. Rev.* **2018**, *180*, 60–91. [CrossRef]
20. Merghadi, A.; Yunus, A.P.; Dou, J.; Whiteley, J.; ThaiPham, B.; Bui, D.T.; Avtar, R.; Abderrahmane, B. Machine Learning Methods for Landslide Susceptibility Studies: A Comparative Overview of Algorithm Performance. *Earth-Sci. Rev.* **2020**, *207*, 103225. [CrossRef]
21. Kavzoglu, T.; Kutlug Sahin, E.; Colkesen, I. An Assessment of Multivariate and Bivariate Approaches in Landslide Susceptibility Mapping: A Case Study of Duzkoy District. *Nat. Hazards* **2015**, *76*, 471–496. [CrossRef]
22. Jessee, M.A.N.; Hamburger, M.W.; Allstadt, K.; Wald, D.J.; Robeson, S.M.; Tanyas, H.; Hearne, M.; Thompson, E.M. A Global Empirical Model for Near-Real-Time Assessment of Seismically Induced Landslides. *J. Geophys. Res.-Earth Surf.* **2018**, *123*, 1835–1859. [CrossRef]
23. Nowicki, M.A.; Wald, D.J.; Hamburger, M.W.; Hearne, M.; Thompson, E.M. Development of a Globally Applicable Model for near Real-Time Prediction of Seismically Induced Landslides. *Eng. Geol.* **2014**, *173*, 54–65. [CrossRef]
24. Ayalew, L.; Yamagishi, H. The Application of GIS-Based Logistic Regression for Landslide Susceptibility Mapping in the Kakuda-Yahiko Mountains, Central Japan. *Geomorphology* **2005**, *65*, 15–31. [CrossRef]

25. Kritikos, T.; Robinson, T.R.; Davies, T.R.H. Regional Coseismic Landslide Hazard Assessment without Historical Landslide Inventories: A New Approach. *J. Geophys. Res. Earth Surf.* **2015**, *120*, 711–729. [CrossRef]
26. Tanyas, H.; Rossi, M.; Alvioli, M.; van Westen, C.J.; Marchesini, I. A Global Slope Unit-Based Method for the near Real-Time Prediction of Earthquake-Induced Landslides. *Geomorphology* **2019**, *327*, 126–146. [CrossRef]
27. Cui, Y.; Bao, P.; Xu, C.; Ma, S.; Zheng, J.; Fu, G. Landslides Triggered by the 6 September 2018 Mw 6.6 Hokkaido, Japan: An Updated Inventory and Retrospective Hazard Assessment. *Earth Sci. Inf.* **2021**, *14*, 247–258. [CrossRef]
28. Chen, W.; Xie, X.; Wang, J.; Pradhan, B.; Hong, H.; Bui, D.T.; Duan, Z.; Ma, J. A Comparative Study of Logistic Model Tree, Random Forest, and Classification and Regression Tree Models for Spatial Prediction of Landslide Susceptibility. *Catena* **2017**, *151*, 147–160. [CrossRef]
29. Fan, X.; Yunus, A.P.; Scaringi, G.; Catani, F.; Siva Subramanian, S.; Xu, Q.; Huang, R. Rapidly Evolving Controls of Landslides After a Strong Earthquake and Implications for Hazard Assessments. *Geophys. Res. Lett.* **2021**, *48*, e2020GL090509. [CrossRef]
30. He, Q.; Wang, M.; Liu, K. Rapidly Assessing Earthquake-Induced Landslide Susceptibility on a Global Scale Using Random Forest. *Geomorphology* **2021**, *391*, 107889. [CrossRef]
31. Luo, X.; Ma, Q.; Niu, F.; Su, W.; Hu, H. Experimental and Numerical Analyses of Freezing Behavior of an Embankment in Cold Regions. *Math. Probl. Eng.* **2019**, *2019*, 1437904. [CrossRef]
32. Achu, A.L.; Aju, C.D.; Di Napoli, M.; Prakash, P.; Gopinath, G.; Shaji, E.; Chandra, V. Machine-Learning Based Landslide Susceptibility Modelling with Emphasis on Uncertainty Analysis. *Geosci. Front.* **2023**, *14*, 101657. [CrossRef]
33. Arabameri, A.; Saha, S.; Roy, J.; Chen, W.; Blaschke, T.; Tien Bui, D. Landslide Susceptibility Evaluation and Management Using Different Machine Learning Methods in The Gallicash River Watershed, Iran. *Remote Sens.* **2020**, *12*, 475. [CrossRef]
34. Di Napoli, M.; Carotenuto, F.; Cevasco, A.; Confuorto, P.; Di Martire, D.; Firpo, M.; Pepe, G.; Raso, E.; Calcaterra, D. Machine Learning Ensemble Modelling as a Tool to Improve Landslide Susceptibility Mapping Reliability. *Landslides* **2020**, *17*, 1897–1914. [CrossRef]
35. Jibson, R.W. Regression Models for Estimating Coseismic Landslide Displacement. *Eng. Geol.* **2007**, *91*, 209–218. [CrossRef]
36. Micheletti, N.; Foresti, L.; Robert, S.; Leuenberger, M.; Pedrazzini, A.; Jaboyedoff, M.; Kanevski, M. Machine Learning Feature Selection Methods for Landslide Susceptibility Mapping. *Math. Geosci.* **2014**, *46*, 33–57. [CrossRef]
37. Robinson, T.R.; Rosser, N.; Walters, R.J. The Spatial and Temporal Influence of Cloud Cover on Satellite-Based Emergency Mapping of Earthquake Disasters. *Sci. Rep.* **2019**, *9*, 12455. [CrossRef]
38. Burrows, K.; Walters, R.J.; Milledge, D.; Densmore, A.L. A Systematic Exploration of Satellite Radar Coherence Methods for Rapid Landslide Detection. *Nat. Hazards Earth Syst. Sci.* **2020**, *20*, 3197–3214. [CrossRef]
39. Burrows, K.; Walters, R.J.; Milledge, D.; Spaans, K.; Densmore, A.L. A New Method for Large-Scale Landslide Classification from Satellite Radar. *Remote Sens.* **2019**, *11*, 237. [CrossRef]
40. Xu, C.; Xu, X.; Shyu, J.B.H.; Zheng, W.; Min, W. Landslides Triggered by the 22 July 2013 Minxian-Zhangxian, China, Mw 5.9 Earthquake: Inventory Compiling and Spatial Distribution Analysis. *J. Asian Earth Sci.* **2014**, *92*, 125–142. [CrossRef]
41. Huang, Y.; Xie, C.; Li, T.; Xu, C.; He, X.; Shao, X.; Xu, X.; Zhan, T.; Chen, Z. An Open-Accessed Inventory of Landslides Triggered by the MS 6.8 Luding Earthquake, China on September 5, 2022. *Earthq. Res. Adv.* **2023**, *3*, 100181. [CrossRef]
42. Zhao, B.; Li, W.; Su, L.; Wang, Y.; Wu, H. Insights into the Landslides Triggered by the 2022 Lushan Ms 6.1 Earthquake: Spatial Distribution and Controls. *Remote Sens.* **2022**, *14*, 4365. [CrossRef]
43. Konishi, T.; Suga, Y. Landslide Detection Using COSMO-SkyMed Images: A Case Study of a Landslide Event on Kii Peninsula, Japan. *Eur. J. Remote Sens.* **2018**, *51*, 205–221. [CrossRef]
44. Yun, S.-H.; Hudnut, K.; Owen, S.; Webb, F.; Simons, M.; Sacco, P.; Gurrola, E.; Manipon, G.; Liang, C.; Fielding, E.; et al. Rapid Damage Mapping for the 2015 Mw 7.8 Gorkha Earthquake Using Synthetic Aperture Radar Data from COSMO–SkyMed and ALOS-2 Satellites. *Seismol. Res. Lett.* **2015**, *86*, 1549–1556. [CrossRef]
45. Han, G.; Dai, D.; Li, Y.; Xi, N.; Sun, L. Rapid Report of the December 18, 2023 MS 6.2 Jishishan Earthquake, Gansu, China. *Earthq. Res. Adv.* **2024**, *4*, 100287. [CrossRef]
46. Chen, B.; Song, C.; Chen, Y.; Li, Z.; Yu, C.; Liu, H.; Jiang, H.; Liu, Z.; Cai, X.; Nai, Y.; et al. Emergency Identification and Influencing Factor Analysis of Coseismic Landslides and Building Damages Induced by the 2023 Ms 6.2 Jishishan (Gansu, China) Earthquake. *Geomat. Inf. Sci. Wuhan Univ.* **2024**, 1–26. [CrossRef]
47. Liu, Z.; Han, B.; Nai, Y.; Li, Z.; Yu, C.; Song, C.; Chen, B.; Zhao, L.; Zahng, X.; Peng, J. Source Parameters and Slip Distribution of the 2023 Mw 6.0 Jishishan (Gansu, China) Earthquake Constrained by InSAR Observations. *Geomat. Inf. Sci. Wuhan Univ.* **2024**, 1–13. [CrossRef]
48. Li, Z.; Li, Y.; Tian, Q.; Xia, Y.; Zhang, J.; Yao, S.; Huang, W. Study on the Relationship between Paleoseismic on Laji Mountain Fault and Catastrophic Event on Lajiashan Site. *J. Seismol. Res.* **2014**, *37*, 109–115.
49. Wang, L.; Hou, S.; Dong, Y.; Tie, Y.; Zhang, M.; Yang, X.; Xiao, R.; Liu, M.; Feng, Z.; Zhang, Y.; et al. Basic characteristics of co-seismic geological hazards induced by Jishishan Ms 6.2 earthquake and suggestions for their risk control. *Chin. J. Geol. Hazard Control* **2024**, *35*, 108–118. [CrossRef]
50. Xu, C.; Xu, X.; Yao, X.; Dai, F. Three (Nearly) Complete Inventories of Landslides Triggered by the May 12, 2008 Wenchuan Mw 7.9 Earthquake of China and Their Spatial Distribution Statistical Analysis. *Landslides* **2014**, *11*, 441–461. [CrossRef]
51. Xu, C.; Xu, X.; Shyu, J.B.H. Database and Spatial Distribution of Landslides Triggered by the Lushan, China Mw 6.6 Earthquake of 20 April 2013. *Geomorphology* **2015**, *248*, 77–92. [CrossRef]

52. Tanyas, H.; van Westen, C.J.; Allstadt, K.E.; Jessee, M.A.N.; Gorum, T.; Jibson, R.W.; Godt, J.W.; Sato, H.P.; Schmitt, R.G.; Marc, O.; et al. Presentation and Analysis of a Worldwide Database of Earthquake-Induced Landslide Inventories. *J. Geophys. Res.-Earth Surf.* **2017**, *122*, 1991–2015. [CrossRef]
53. Deng, Q. *Active Structure Map of China (1:400,000)(with CD)*; Earthquake Press: Beijing, China, 2007.
54. Dijkshoorn, K.; van Engelen, V.; Huting, J. *Soil and Landform Properties for LADA Partner Countries (Argentina, China, Cuba, Senegal and The Gambia, South Africa and Tunisia)*; ISRIC report 2008/06 and GLADA report 2008/03; ISRIC—World Soil Information and FAO: Wageningen, The Netherlands, 2008.
55. Yamazaki, D.; Ikeshima, D.; Sosa, J.; Bates, P.D.; Allen, G.H.; Pavelsky, T.M. MERIT Hydro: A High-Resolution Global Hydrography Map Based on Latest Topography Dataset. *Water Resour. Res.* **2019**, *55*, 5053–5073. [CrossRef]
56. Yamazaki, D.; Ikeshima, D.; Tawatari, R.; Yamaguchi, T.; O'Loughlin, F.; Neal, J.C.; Sampson, C.C.; Kanae, S.; Bates, P.D. A High-Accuracy Map of Global Terrain Elevations. *Geophys. Res. Lett.* **2017**, *44*, 5844–5853. [CrossRef]
57. Zhang, X.; Liu, L.; Chen, X.; Gao, Y.; Xie, S.; Mi, J. GLC_FCS30: Global Land-Cover Product with Fine Classification System at 30m Using Time-Series Landsat Imagery. *Earth Syst. Sci. Data* **2021**, *13*, 2753–2776. [CrossRef]
58. China Geological Survey Xi'an Geological Survey Center; China Natural Resources Inspector Xi'an Bureau. *Atlas of Natural Resources in the Middle and Upper Yellow River Basin of China*; Xi'an Bureau, State Natural Resources Inspector: Xi'an, China; China University of Geosciences Press: Wuhan, China, 2021; ISBN 978-7-5625-5061-7.
59. Zeng, T.; Wu, L.; Peduto, D.; Glade, T.; Hayakawa, Y.S.; Yin, K. Ensemble Learning Framework for Landslide Susceptibility Mapping: Different Basic Classifier and Ensemble Strategy. *Geosci. Front.* **2023**, *14*, 101645. [CrossRef]
60. Zhou, Z.-H.; Feng, J. Deep Forest. *Natl. Sci. Rev.* **2019**, *6*, 74–86. [CrossRef]
61. Chen, T.; Guestrin, C. XGBoost: A Scalable Tree Boosting System. In Proceedings of the 22nd ACM SIGKDD International Conference on Knowledge Discovery and Data Mining; Association for Computing Machinery: New York, NY, USA, 2016; pp. 785–794.
62. Huang, Y.; Zhao, L. Review on Landslide Susceptibility Mapping Using Support Vector Machines. *Catena* **2018**, *165*, 520–529. [CrossRef]
63. Huang, F.; Cao, Z.; Guo, J.; Jiang, S.-H.; Li, S.; Guo, Z. Comparisons of Heuristic, General Statistical and Machine Learning Models for Landslide Susceptibility Prediction and Mapping. *Catena* **2020**, *191*, 104580. [CrossRef]
64. Lin, G.; Chang, M.; Huang, Y.; Ho, J. Assessment of Susceptibility to Rainfall-Induced Landslides Using Improved Self-Organizing Linear Output Map, Support Vector Machine, and Logistic Regression. *Eng. Geol.* **2017**, *224*, 62–74. [CrossRef]
65. Rother, C.; Minka, T.; Blake, A.; Kolmogorov, V. Cosegmentation of Image Pairs by Histogram Matching—Incorporating a Global Constraint into MRFs. In Proceedings of the 2006 IEEE Computer Society Conference on Computer Vision and Pattern Recognition (CVPR'06), New York, NY, USA, 17–22 June 2006; Volume 1, pp. 993–1000.
66. Nguyen, H.V.; Bai, L. Cosine Similarity Metric Learning for Face Verification. In Proceedings of the Computer Vision—ACCV 2010; Kimmel, R., Klette, R., Sugimoto, A., Eds.; Springer: Berlin/Heidelberg, Germany, 2011; pp. 709–720.
67. Gonzalez, R.; Woods, R. *Digital Image Processing: Global Edition*; Pearson Deutschland: Munich, Germany, 2017; ISBN 978-1-292-22304-9.
68. Wang, Z.; Liu, J.; Che, X.; Wang, Y.; Du, K. Research on map similarity matching method based on convolutional neural network. *Sci. Surv. Mapp.* **2022**, *47*, 169–175. [CrossRef]
69. Wang, H.; Huang, Y.; Cai, B. Comparison of Image Similarity Algorithms Based on Traditional Methods and Deep Learning Methods. *Comput. Syst. Appl.* **2024**, *33*, 253–264. [CrossRef]
70. Xian, Y.; Wei, X.; Zhou, H.; Chen, N.; Liu, Y.; Liu, F.; Sun, H. Snowmelt-Triggered Reactivation of a Loess Landslide in Yili, Xinjiang, China: Mode and Mechanism. *Landslides* **2022**, *19*, 1843–1860. [CrossRef]
71. Gao, Y.; Xu, J.; Zhang, M.; Jiang, F. Advances in the Study of the 400 Mm Isohyet Migrations and Wetness and Dryness Changes on the Chinese Mainland. *Adv. Earth Sci.* **2020**, *35*, 1101. [CrossRef]
72. Zhang, S.; Sun, P.; Li, R.; Wang, F. Preliminary Investigation on a Catastrophic Loess Landslide Induced by Heavy Rainfall on 1 September 2022 in Qinghai, China. *Landslides* **2023**, *20*, 1553–1559. [CrossRef]
73. Stamatopoulos, C.A.; Protopapas, A.L. Analytical Solutions for the Sliding Displacement of Model Slopes Simulating Both the Frictional and Rotational Effects under Piecewise Linear Acceleration Pulses. *Earthq. Eng. Struct. Dyn.* **2023**, *52*, 4733–4753. [CrossRef]
74. Gallen, S.F.; Clark, M.K.; Godt, J.W. Coseismic Landslides Reveal Near-Surface Rock Strength in a High-Relief, Tectonically Active Setting. *Geology* **2015**, *43*, 11–14. [CrossRef]

Disclaimer/Publisher's Note: The statements, opinions and data contained in all publications are solely those of the individual author(s) and contributor(s) and not of MDPI and/or the editor(s). MDPI and/or the editor(s) disclaim responsibility for any injury to people or property resulting from any ideas, methods, instructions or products referred to in the content.